# Volborthite and Its Composite with g-$C_3N_4$ for Oxytetracycline Removal: Their Adsorption and Photocatalysis Properties

**Wei Qing Wee**
Universiti Tunku Abdul Rahman
**Lan Ching Sim**
simlc82@yahoo.com
Universiti Tunku Abdul Rahman https://orcid.org/0000-0003-4002-6726
**Kah Hon Leong**
Universiti Tunku Abdul Rahman
**Azrina Abdul Aziz**
Universiti Malaysia Pahang: Universiti Malaysia Pahang Al-Sultan Abdullah

**Research Article**

**Keywords:** Volborthite, Copper vanadate, g-C3N4, Adsorption, Photocatalysis, Oxytetracycline

**Posted Date:** February 2nd, 2024

**DOI:** https://doi.org/10.21203/rs.3.rs-3692401/v1



**Version of Record:** A version of this preprint was published at Environmental Science and Pollution Research on March 11th, 2024. See the published version at https://doi.org/10.1007/s11356-024-32802-3.

# Abstract

The photocatalytic-adsorption performance of the composites of volborthite (CuVA) and graphitic carbon nitride (g-$C_3N_4$) was studied in this work using oxytetracycline (OTC) as model pollutant under LED light irradiation. CuVA at different weight percentage (10, 30, 50), namely C10, C30 and C50 were loaded onto graphitic carbon nitride using wet chemical method. The physical, chemical and optical properties were evaluated *via* various analytical techniques. Through integrated adsorption-photocatalytic process, no significant photocatalytic reaction occurred in g-$C_3N_4$ and the composite even after 4 h of irradiation. The setup was modified such that each run was conducted in the presence and absence of light. Aside from photolysis and g-$C_3N_4$, all composites performed better under the presence of light in which CuVA improved the most from ~50% down to ~20% of initial concentration. CuVA performed almost identically (80% removal of OTC) under the presence of light irradiation at ambient temperature (22 °C) and in the dark at 32 °C, confirming that temperature was the contributing factor to the improvement instead of light. CuVA exhibited excellent adsorption capacity of 171 mg/g and adsorption rate of 90% towards the removal of highly concentrated OTC (100 mg/L) under optimized parameters of pH 5.0 and at 42 °C after 3 h of adsorption process. Life cycle assessment revealed that close to 50% of fresh 100 ppm OTC could be removed after 5 cycles without any desorption process.


# Introduction

Over the past half-century, the usage of oxytetracycline (OTC) has been increased with the development of livestock breeding and aquaculture. However, majority of the administered antibiotics are being excreted as original compounds into the environment (Li a., 2019). This large introduction of antibiotics may potentially destroy the natural microbial ecological community as well as the animal up the food chain (Kraemer, Ramachandran and Perron, 2019). In particular, OTC has low volatility and extremely soluble in water (Lin et al., 2022). This result in the pollutant being difficult to separate in its solution form through conventional wastewater treatment method. Removal of OTC from ambient environment is crucial as these residues promotes mutation of antibiotic resistant microorganism, reducing the effect of said antibiotics (Mog et al., 2020). Adsorption and photocatalysis are both promising technology for removing stable pollutants from water. However, photocatalyst are usually nanoparticle sized thus is very costly to be separated from solution after use, especially when the volume is large. Moreover, photocatalyst are prone to agglomeration due high surface energy (Chairungsri et al., 2022) and the reaction rate of photocatalysis is slow. On the other hand, adsorbent often have trouble with regeneration and disposal (Tan et al., 2020). Using porous and large surface area characteristic of adsorbent, the nanoparticle of photocatalyst may be distributed evenly and fixed onto the surface. The high adsorptive ability and porous structure keeps the pollutant molecules near the active sites of photocatalyst, enhancing the performance and lowering the generation of by-products (Long et al., 2021). By integrating these two mechanisms together, the adsorption process can probe the pollutants onto substrate surface to increase the reaction rate of photocatalysis. At the same time, photocatalysis process will degrade the

pollutants into $CO_2$ and $H_2O$, thus regenerating the adsorbent. Such coupling mechanisms could provide a high potential to the practical applications of photocatalysis.

When photocatalyst being deployed alone, the reaction may be incomplete, generating by-products that will aggregate on the surface, blocking the active sites and thus reducing the performance over time (Isari et al., 2020). As a result, there is a balance needed when selecting materials to be combine. Graphitic carbon nitride (g-$C_3N_4$) as a non-metal photocatalyst with high thermal and chemical stability have been studied extensively in degradation of dye, organic pollutant, and hydrogen evolution (Vignesh et al., 2022). However, commercialization is still unfeasible without solving the high recombination rate of electron-hole pairs and slow reaction rate. Several adsorption-photocatalysis g-$C_3N_4$ based hybrid materials such as adsorbent-g-$C_3N_4$ hybrid material, g-$C_3N_4$-adsorptive photocatalyst and modified g-$C_3N_4$ and its heterojunction were attempted to realize the idea of integrated materials (Yu and Huang, 2023). Yu et al. (2020) fabricated a hybrid $TiO_2/SiO_2$/g-$C_3N_4$ composite using ternary-soft-template method. The removal rate of berberine hydrochloride (BH) using the composite was 2.63 time than that of g-$C_3N_4$ after 60 min of adsorption-photocatalytic reaction. The flower-like microsphere $SiO_2$ could provide a higher specific surface and lead to a higher adsorption rate of BH. While $TiO_2$/g-$C_3N_4$ heterojunction could promote in situ photocatalytic degradation of the adsorbed BH. Jiang et al. (2016) reported adsorptive photocatalyst namely polyaniline/g-$C_3N_4$ nanosheets composite hydrogel with 3D hierarchical nanostructure which removed 89.1% and 84% of methylene blue and phenol, respectively. Similar hybrid mechanism was observed in which polyaniline hydrogel adsorbed the pollutants and degraded by polyaniline/g-$C_3N_4$ heterojunction. Modified g-$C_3N_4$ with two-dimensional (2D) or three-dimensional (3D) structures is extensively employed due to its higher specific surface area and good adsorption ability. Chen et al. (2023) synthesized 3D porous $CeO_2$/g-$C_3N_4$ composite using one step calcination and achieved 88.4% of tetracycline removal efficiency through adsorption-photocatalytic mechanism. They found that 55% of tetracycline was removed by adsorption which indicates that adsorption is the dominant mechanism.

In parallel with the efforts on binary metal oxide, the focus is recently shifted to multinary metal oxide semiconductor which have been widely studied for water splitting (Song et al., 2023; Fawzy et al., 2019), energy storage and conversion (Xie et al., 2023; Zequine et al., 2019) and degradation of pollutant (Kamble and Ling, 2020; Thendral et al., 2023). The multinary metal oxide consists of multiple type of metal oxide, for example, vanadate-based molecule containing $Ag_2O$, $Bi_2O_3$, $In_2O_3$ or CuO. Copper vanadate-based material in particular have multiple type of arrangement ($Cu_3V_2O_7$, $Cu_2V_2O_7$, $CuV_2O_6$, etc.). This is caused by vanadium, being a multivalent element, can undergo oxidation to various oxidation states by manipulating conditions such as temperature, pressure, and density (Liang et al., 2012). This difference in arrangement of structure alters the bandgap, recombination rates and photocurrent density of the materials, which in turns contributes to varying photocatalytic performance (Wang et al., 2018). Volborthite ($Cu_3V_2O_7(OH)_2 \cdot 2H_2O$) is a hydrated form of copper vanadate, it has a unique Kagome lattice structure containing CuO (octahedra), $V_2O_5$ (tetrahedra) and crystal $H_2O$ molecule

(Hiroi et al., 2019). The main advantage of volborthite over other copper vanadate phase is that it does not require high temperature annealing post-synthesis. This allows the synthesis of volborthite to be much simpler. It could be a potential to surpass other adsorbents and photocatalyst. Song et al. (2022) studied a heterostructure consists of volborthite, copper oxide and metallic copper as semiconductor for $CO_2$ reduction. They found that volborthite was showing good visible light response when measured using UV-vis spectrometer. When copper oxide is introduced, the composites showed further enhancement in near-infrared range. In their study, pristine volborthite showed zero yield of $CH_4$ while CO is being produced at 0.55 μmol/g/h. At 13.1 wt% copper oxide and 9.4 wt% metallic copper, the sample was significantly improved, at 6.97 and 1.64 μmol/g/h of $CH_4$ and CO generation, respectively. This improvement may be contributed by heterojunction interaction between the three components, which was confirmed by photoluminescence (PL) spectra, photocurrent response, and electrochemical impedance spectra (EIS) result (Song et al., 2022).

This research work focuses on the investigation of the feasibility of using volborthite (CuVA) and g-$C_3N_4$ composite, namely CuVA/g-$C_3N_4$ for the removal of high concentration OTC (100 mg/L) under LED light irradiation. Different weight percentage of CuVA (10, 30 and 50 wt%) was incorporated into g-$C_3N_4$ and the as-prepared composites were evaluated together with comparison with CuVA and g-$C_3N_4$ by investigating their removal efficiency towards the OTC. To the best of our knowledge, little attention has been paid on applications of CuVA and its family of composite in hydrated form. Besides, most of the reported work adopted lower range of OTC concentration (10 mg/L) as pollutant model (Senasu et al., 2023; Chin et al., 2023; Cheng et al., 2023) whereas higher range of OTC concentration is seldom reported. These factors necessitate the elucidation of the prominent role of CuVA and g-$C_3N_4$ in the integrated system for the removal of highly concentrated OTC. The prepared samples were characterized to examine the materials' innate physical and chemical properties. Integrated photocatalytic-adsorption process was adopted to remove OTC at first but the photocatalytic efficiency was insignificant after achieving adsorption-desorption equilibrium. Hence, OTC removal performance was conducted separately in the dark adsorption and irradiation of light to identify the best performing sample, in this case, CuVA. Upon discovery, CuVA is excel in removing OTC through adsorption and the direction had moved to study the adsorption behavior of CuVA, this includes effect of pH, temperature and presence of light. This is followed by kinetic and isotherm modelling, thermodynamic study and finally, life cycle assessment on CuVA. This study could provide a new insight towards the current state-of-art removal of highly concentrated OTC.

# Experimental

# Materials

All the chemical reagents were of analytical grade and used without any further purification. Urea (99.0-100.5%, Fisher Scientific), copper (II) nitrate trihydrate ($Cu(NO_3)_2{\cdot}3H_2O$, ≥ 99.0, R&M chemicals),

ammonium metavanadate ($NH_4VO_3$, ≥ 99.0, Sigma-Aldrich) and oxytetracycline hydrochloride ($C_{22}H_{24}N_2O_9$·HCl, 94.5–102%, Sigma-Aldrich).

# Synthesis of g-$C_3N_4$

Bulk g-$C_3N_4$ was synthesized by thermal polymerization of urea. In a typical procedure, 20 g of urea were placed into an alumina crucible with a cover, wrapped with aluminium foil and heated up to 580°C for 4 h at heating rate of 10°C (Hak et al., 2020). Wrapping is necessary as the ammonia vapor generated from decomposition of urea is crucial for the formation of g-$C_3N_4$, without covering, the vapor will escape, and reaction will not occur. The products were left cooling inside the furnace overnight without control. The pale yellowish products were then collected and crushed into fine powder using pestle and mortar.

# Synthesis of CuVA/g-$C_3N_4$ Composites and Pure CuVA

Different weight percentage of volborthite (CuVA) (10, 30 and 50 wt%) was incorporated into g-$C_3N_4$ using wet chemical method to obtain integrated adsorbent-photocatalyst. It was found that 10 wt% loading will face the issue of lack of active species and limited light absorbance region, 50 wt% loading will encounter the issue of aggregation and blocking the surface of g-$C_3N_4$. On the other hand, 30 wt% could produce enough photoactive species while did not block the surface of g-$C_3N_4$ (Ye et al., 2016). Hence, specific weight percentage of 10, 30 and 50 wt% were chosen to represent little, moderate, high loading of CuVA on g-$C_3N_4$. The obtained samples were named as C10, C30 and C50, respectively. Using C50 as example, 81.697 mg of g-$C_3N_4$ were dispersed into 125 mL of 5 mM $Cu(NO_3)_2·3H_2O$ solution through sonication for 5 min. Next, 125 mL of 5 mM $NH_4VO_3$ were added dropwise into the suspension at room temperature and the mixture was adjusted to pH 7. The suspension was ultrasonicated for 40 min for CuVA to crystallize. The obtained precipitate was centrifuged at 10,000 rpm and washed multiple times with distilled water and 99% isopropanol. The solids were then dried at 80°C overnight to obtain the final products. C10 and C30 was prepared following the similar route. The feed quantity of g-$C_3N_4$ for each composite was adjusted according to the mass ratio and yield of CuVA. Pure CuVA was synthesized using the exact method without adding g-$C_3N_4$ during the preparation procedure.

# Characterization

Morphology and composition of samples were evaluated by field emission scanning electron microscopy (FESEM), performed on a JEOL JSM6701F and transmission electron microscopy (TEM) (LIBRA 120, Carl Zeiss NTS GmbH) equipped with an energy dispersive X-ray spectrometer (EDX). The crystalline and phase compositions were analyzed by X-ray diffraction (XRD, Shimadzu XRD-6000) with Cu Kα radiation λ = 0.154 nm. Fourier transform infrared (FT-IR) spectra (400–4000 $cm^{-1}$) of samples were recorded on a Nicolet IS10 at room temperature. UV-vis diffuse reflectance spectra (DRS) were performed through Perkin Elmer, Lambda 950. Time-resolved photoluminescence (TRPL) was performed on an Edinburgh FLS-920 with excitation wavelength at 376.4 nm and emission wavelength at 450 nm to obtain the recombination time. Specific surface area of the samples was evaluated using Brunauer, Emmett and

Teller (BET) theory on a Micromeritics 3Flex using nitrogen adsorption at 77 K. Sample was degassed at 120°C for 180 min with a ramping rate of 10°C/min before undergoing adsorption analysis. X-ray photoelectron spectroscopy (XPS) was performed using Shimadzu, AXIS ULTRA DLD. The sample surface was excited using aluminium monochromatic X-ray source (Al Kα).

# Removal of Oxytetracycline in Absence and Presence of Light Irradiation

Integrated photocatalytic-adsorption process was adopted to remove OTC in which dark adsorption was carried out for 16 h, followed by the photocatalysis process. Since the photocatalytic efficiency was plateau after reaching adsorption-desorption equilibrium (Fig. S2), OTC removal performance was studied separately in the absence and presence of light irradiation. The adsorption efficiency of OTC was studied using the composite of CuVA/g-$C_3N_4$ (C10, C30 and C50) in the dark condition. Using C10 as example, 100 mg of C10 was added into 200 mL OTC solution (100 mg/L) and stirred in the dark. The OTC sample was collected at 0, 30, 60, 90, 120, 150, 180, 240, 300, 360 min. Similar steps were repeated for C30, C50, g-$C_3N_4$ and CuVA. In photocatalytic process, 100 mg/L of OTC was prepared, and the solution was adjusted to pH 5. Using C10 as example, 100 mg of C10 was introduced into the prepared 200 mL OTC solution and 30 W LED light (Philips) was switched on. The distance of the light bulb to the surface of the solution is fixed at 10 cm. Aliquot (3 mL) of samples was collected and filtered using a 0.21 μm syringe filter to remove all the solid. The whole procedure was conducted at room temperature of 22°C for 360 min and the similar steps were repeated for g-$C_3N_4$, C30, C50 and CuVA as comparison. The concentrations of OTC were examined using UV-vis spectrophotometer (Agilent Cary 100) at maximum absorbance wavelengths of 274 nm. Further studies were carried out for the dominant process contributing to the removal of OTC.

# Effect of Temperature and pH

Herein, the effect of temperature and pH was investigated using the best adsorption performance sample, CuVA. The effect of temperature and pH on removal efficiency of OTC through adsorption was studied using the similar setup as adsorption process. The effect of temperature was studied by varying the solution temperature at 22°C, 27°C, 32°C, 37°C and 42°C. Study on blank OTC solution was first conducted to confirm the thermal stability of OTC under these temperature conditions. Using the kinetics obtained, the activation energy can be obtained using Arrhenius equation. The effect of pH was studied by varying the solution initial pH at pH 2.0, 5.0, 8.5 and 11.0. Initial pH of the OTC solution was adjusted using 0.5 M ammonia and 0.5 M HCl solution. Study on OTC solution without samples were first conducted to confirm the pH stability of OTC under these pH conditions.

# Reusability Test

The reusability of CuVA was evaluated in five cycling experiments, with the removal of OTC under the same reaction condition (100 mg of sample dispersed in 100 ppm OTC solution at pH 5 and 42°C). At the end of each cycle, the spent solutions were centrifuged at 10,000 rpm to recover the samples and washed

with water and ethanol, followed by oven drying at 80°C overnight. The recovered samples were applied for the next cycle.

## Results and Discussion

# Characterization

Before performing any characterization technique, the increase in wt% of CuVA on g-$C_3N_4$ can be observed physically based on the colour shift of the powder synthesized (Fig. S1). As the wt% of CuVA increases, the intensity of green grows. The powder presented in green is also a preliminary indication of synthesis of copper vanadate in its hydrated form is successful, as the dehydrated form of copper vanadate ($Cu_2V_2O_7$) is red in colour (Khan and Qurashi, 2017). From Fig. 1(a), CuVA appears to have needle or rod-like structure while bulk g-$C_3N_4$ appears with sheet-like structure (Fig. 1(b)). As shown in Fig. 1(c)-(e), CuVA was successfully incorporated onto surface of g-$C_3N_4$. Crystalline size of CuVA did not seem to be affected by the introduction of nucleation point by g-$C_3N_4$. Moreover, the distribution of CuVA on the surface of g-$C_3N_4$ appears to be more uniform instead of agglomerating like the pristine CuVA. The elemental EDX analysis (Table S1) detecting the presence of Cu, V, O, C and N, further indicating the successful incorporation of CuVA onto g-$C_3N_4$ in an increasing trend. Presence of carbon in CuVA could be contributed by carbon tape background or impurities as calcination process were not conducted during the synthesis process. Calcination was not conducted as it will alter the chemical structure of CuVA into its dehydrated form (Khan and Qurashi, 2017). Presence of oxygen in g-$C_3N_4$ was contributed by the unreacted residue of intermediate product during pyrolysis of urea (Feng et al., 2017).

The surface morphologies of prepared C50 and CuVA were examined using HRTEM analyses. Figure 2(a) demonstrated that CuVA nanoparticles were deposited on the lamellar sheet like morphological structure of g-$C_3N_4$. On the other hand, CuVA exhibit rod like morphologies with lattice fringes ranging from 0.70 to 0.78 nm as shown in Fig. 2(b) and (c). These interplanar spacing values were indexed to (0 0 1) plane of CuVA (Song et al., 2022). Morphologies of both samples in distinctive shape agrees with the previous observation from FESEM image. The single crystalline nature of CuVA was also confirmed from the lattice fringes as the lattice fringe is facing one direction. The particle size of CuVA ranges from 70 nm to 150 nm with an average length of 111.04 nm (Fig. 2(d)), confirming that CuVA was successfully synthesized in nanosized.

As revealed by XRD in Fig. 3(a), the typical peaks of CuVA are well-indexed to the monoclinic phase of $Cu_3V_2O_7(OH)_2{\cdot}2H_2O$ and they are in accordance with the JCPDS card no. 80-1169 (Jain et al., 2020). The sample has high purity and well crystallinity with crystallite diameter of 27.7 nm. On the other hand, the as prepared g-$C_3N_4$ showed two pronounced peaks at 13.1° and 28.33°, which are in accordance with the JCPDS card no. 87-1526. The major peak at 13.1° represent the in-plane tri-s-triazine unit with (1 0 0) diffraction while the peak at 28.33° represent the aromatic C-N unit with (0 0 2) diffraction (Modwi et al., 2023). The peaks of CuVA become more apparent as the wt% increases, signifying the introduction of

CuVA onto g-$C_3N_4$ were successful and the trend is positive. The typical diffraction peak of CuVA in each sample remain almost unchanged, suggesting that the crystal lattice of CuVA was not affected during the fabrication process of CuVA/g-$C_3N_4$ composites.

FTIR spectrum of CuVA/g-$C_3N_4$ composites (Fig. 3(b)) shows the surface functional group of as prepared composite. For CuVA, V-O-V and V-O can be observed at 841 $cm^{-1}$ and 1018 $cm^{-1}$ (Sánchez-Loredo et al., 2023). Asymmetric vibration of V-O-Cu and V-O-V at 764 $cm^{-1}$ and weak band at 524 $cm^{-1}$ contributed by Cu-O (Bayat et al., 2018). On the other hand, for g-$C_3N_4$, the broad-band present around 3000–3500 $cm^{-1}$ is due to stretching vibrations of uncondensed primary (-NH-) and secondary (-$NH_2$) amines present in residual amino groups on the edges of CN heterocycles. The fingerprint region presented near 1150–1750 $cm^{-1}$ can be ascribed to C-N and C ≡ N stretching vibration unit of CN aromatic repeating unit (Benisti et al., 2021). Peak observed at 880 and 810 $cm^{-1}$ is contributed by the out-of-plane vibrations of triazine or s-triazine repeating units (Pareek et al., 2018). As weight percentage of CuVA increases from 10 wt% to 50 wt%, a minor decrease in intensity near 841 $cm^{-1}$ is observed. This is contributed by V-O-Cu (region b). The changes in spectra with the introduction of CuVA onto g-$C_3N_4$ are not obvious because g-$C_3N_4$ provides a strong IR intensity near region (2). Based on the FTIR spectra, introduction of CuVA onto g-$C_3N_4$ was successful. Moreover, insignificant changes in the overall spectra contributed by g-$C_3N_4$ indicates that the incorporation process does not alter the molecular structure of g-$C_3N_4$.

The light harvesting capability of samples were measured using UV-vis DRS, and from the Kubelka-Munk transformation of the measurement (Fig. 4(a)), the strength followed the order of CuVA > C50 > C30 > C10 > g-$C_3N_4$. Pure g-$C_3N_4$ exhibit strong absorption band in the region of 300–420 nm and has a sharp adsorption edge up to 420 nm. The strong absorption band is attributed to the π-π* transition of lone pairs of N atoms of triazine/heptazine ring (Ge et al., 2021). On the other hand, CuVA exhibits strong absorption band in the region of 300–560 nm and has a sharp adsorption edge up to 560 nm towards the visible light region of solar spectrum. Small shoulder presented above 600 nm is attributed to partially dehydrated CuVA phase (Wang et al., 2018). Band gap energy was estimated by converting the Kubelka-Munk transformation spectra into Tauc plot. Tauc plot is generated by assuming the energy-dependent absorption coefficient  can be represented by Eq. 1:

$$( \ - h \ )^{1/} = B (h \ - E_g) \quad (1)$$

where h is the Plank constant,  is the photon frequency, $E_g$ is the bandgap, and B is a constant. Depending on the nature of electron transition, the  can be either ½ or 2 for direct and indirect transition band gap respectively. In the case of CuVA/g-$C_3N_4$ composites, direct bandgap showed a better fitting to the plot thus the materials were assumed to have direct bandgap characteristics (Fig. 4(b)-(c)). Band gap of g-$C_3N_4$ was estimated to be 3.05 eV and pristine CuVA was estimated to be around 2.47 eV. The absorption spectra of all composites are red-shifted after the introduction of CuVA onto g-$C_3N_4$. This is

attributed to successful incorporation of CuVA to narrow the band gap energy of g-$C_3N_4$. Using the band gap obtained, their respective valance band (VB) and conduction band (CB) can be calculated using Eqs. 2 and 3:

$$E_{CB} = \chi - E_e + 0.5\,E_g \quad (2)$$

$$E_{VB} = E_{CB} + E_g \quad (3)$$

where $E_{CB}$ and $E_{VB}$ are their respective potentials, $E_e$ is the potential of free electron against hydrogen electrode (4.5 eV), and χ is the electronegativity of semiconductor, and is calculated using Eq. 4:

$$\chi = \left[\mathrm{x(A)}^{a} * \mathrm{x(B)}^{b} * \ldots\right]^{\left(\frac{1}{a+b+\ldots}\right)}$$

4

where A, B are the respective element, a, b are the number of atoms of respective element, and x(Y) is Mulliken's electronegativity of respective element Y with Pauling values and is expressed by Eq. 5:

$$x(Y) = 0.187(E_{I1} + E_{EA}) + 0.17 \quad (5)$$

where $E_{I1}$ is the first ionization energy of the respective element Y (eV/particle), and $E_{EA}$ is the electron affinity of the respective element Y. With the utilization of these equations, the band position of the conduction band (CB) edge and valence band (VB) edge were established.

The results are illustrated in Fig. 4(d), indicating that g-$C_3N_4$ exhibits a CB edge at -1.08 eV and a VB edge at 1.97 eV, while CuVA displays a CB edge at -1.54 eV and a VB edge at 0.93 eV. The position of both CuVA and g-$C_3N_4$ are lower than + 1.98 eV (vs. NHE, pH 7), which is the potential needed to form hydroxyl radicals (●OH) (Baudys et al., 2020). This indicates that the oxidation potential of holes in the VB edge is insufficient to produce ●OH. On the other hand, the position of CB edge of both materials is more negative compares to the potential needed to form superoxide radicals ($^{\bullet}O_2^-$) (-0.33 eV vs. NHE, pH 7) (Giannakopoulou et al., 2017). This indicates that the reduction potential of free electron in CB edge is sufficient to reduce molecular oxygen to form $^{\bullet}O_2^-$. These results suggest that the photocatalytic process using CuVA/g-$C_3N_4$ composites relies solely on $^{\bullet}O_2^-$ due to the unavailability of ●OH, as determined from the band-edge position. From the band-edge position illustrated in Fig. 4(d), provided if heterojunction incorporation is successful, CuVA/g-$C_3N_4$ composite will exist as a Type II heterojunction photocatalyst.

The lifetime of charge carrier was analysed using TRPL. These values were estimated by fitting triple exponential decay function to the data point obtained as shown in Fig. 5(a). The measured lifetime corresponds to the duration it takes for electron-hole pairs to decay to approximately 1/e of their initial quantity (Nagappagari et al., 2021). From the inset, g-$C_3N_4$ has the highest charge-carrier lifetime at 5.75 ns, with decrease in lifetime as loading of CuVA increases. This indicates that the incorporation of CuVA increased the recombination rate of electron-hole pairs which could be detrimental to the overall

photocatalytic properties of the CuVA/g-$C_3N_4$ composites (Nguyen Van et al., 2020). The decrease in emission lifetime in the material suggest a non-radiative pathway from electronic interaction between CuVA and g-$C_3N_4$ (Ye et al., 2016). As shown in Fig. 5(b), all composites exhibit type IV physisorption isotherm that indicates the porous nature of the nanostructured material. The hysteresis loop resembling type H3, suggest that the pore structure resemble wedge with opening at both ends or groove pores formed by flaky particles (Chen et al., 2018). This is in line with the observation from FESEM image where g-$C_3N_4$ possess flaky structure while CuVA possess non-rigid crystal structure. Table 1 indicates that g-$C_3N_4$ possesses the largest surface area at 88.2 $m^2$/g, followed by 83.4, 80.1, 68.7 and 49.4 $m^2$/g for C10, C30, C50 and CuVA, respectively. As the wt% of CuVA increases, specific surface area of composite decreases. Barrett-Joyner-Halenda (BJH) pore size distribution (inset of Fig. 5(b)) calculated from BJH adsorption branch indicates the pore size are majority in the range of around 2.7 nm. As loading of CuVA on g-$C_3N_4$ increases, the calculated pore volume decreases although no shifting in pore width was observed. This phenomenon appears due to CuVA, a relatively smaller sized material is being deposited on the pore of g-$C_3N_4$. Higher overall surface area is often correlated to improve in photocatalytic performance because it exposes more active sites for both physisorption and chemisorption which improves the efficiency of interaction between pollutant and the surface (Amrute et al., 2021).

Table 1
Specific surface area and overall pore volume of g-$C_3N_4$, C10, C30, C50 and CuVA.

| Sample | Specific surface area ($m^2$/g) | Pore Volume ($cm^3$/g) |
|---|---|---|
| g-$C_3N_4$ | 88.2085 | 0.171545 |
| C10 | 83.3924 | 0.171784 |
| C30 | 80.0809 | 0.165875 |
| C50 | 68.7386 | 0.126169 |
| CuVA | 49.3588 | 0.086291 |

# Removal Performance of OTC

Typical adsorption-photocatalytic process involves conducting dark adsorption to achieve adsorption-desorption equilibrium before proceeding to photocatalysis. However, this approach was not viable for our study as no substantial OTC removal was observed after maintaining the dark adsorption for 16 h (Fig. S2). Hence, the removal performance of OTC was conducted separately under dark adsorption (Fig. 6(a)) and light irradiation (Fig. 6(b)). It was observed that CuVA improved the most, and at the same time was the best performing sample, by introducing light into the system, from remaining around 50% in dark to 20% of OTC initial concentration (100 mg/L) after 6 h. Notably, g-$C_3N_4$ which is a well-studied

photocatalyst did not appear to have any significant photocatalytic degradation properties towards OTC as the concentration of OTC remained relatively similar after 6 h. As shown in Fig. 6(c), chemical oxygen demand (COD) of the solution under the influence of light were consistently lower than that of in the absence of light. The COD analysis shows that the solution contained lower amount of organic compound after the reaction in the presence of light. Notably, Fig. 6(d) also shows the solution pH tended to rise after the reaction. It can be observed that the amount of pH increased is correlated to the amount of OTC being removed from the aqueous solution. This phenomenon was caused by OTC, existing as $OTCH_2^{0(+/-)}$ at pH 5.0 were slowly removed from the aqueous solution. Throughout the experimental process to produce Fig. 6(b), under the influence of light, it was observed that temperature of all OTC solution gradually increased and settled at around 32°C with the ambient temperature controlled at 22°C. Since the temperature of OTC solution was not controlled under the presence of light, two possible factors were considered which may contribute to the improvement of performance: presence of light and higher temperature condition.

Using the resources available, eliminating the presence of light by wrapping the solution with aluminium foil and at the same time increased the temperature using a hotplate proof to be easier to setup consistently compared to maintaining the solution temperature to ambient temperature. Through this study, it was discovered that CuVA exhibited excellent adsorption capability towards OTC, and that the removal was adsorption dominated. This was observed through CuVA performing almost identically under the presence of light at ambient temperature and absence of light under 32°C. As shown in Fig. S3, close to 80% of OTC was removed after 6 h. Performance of CuVA in dark while heating performed slightly better than that of CuVA with light irradiation. This behaviour is due to the setup of initial temperature of the solution was fixed at 32°C prior to adding the sample in the dark while for light irradiation, the temperature was slowly raised by the passive heat generated by the LED bulb throughout the experiment. This analysis confirms that the improvement of OTC removal performance in the presence of light was due to the higher temperature condition. Hence, adsorption study on CuVA was further carried out under dark condition to identify the adsorption mechanism towards OTC.

The surface elemental oxidation state binding energies of pristine CuVA and after being used to adsorb OTC (denoted as CuVA R1) were analysed with XPS spectra. The full survey spectrum (Fig. 7(a)) confirmed the presence of Cu 2p, V 2p, O 1s and C 1s elemental peaks. N 1s impurities was observed located near 405 eV for both samples. This is due to the presence of $NH_4^+$ and $NO_3^-$ in each of the precursor during the synthesis of CuVA. Figure 7(b) shows the Cu 2p peaks centred near 932 eV and 952 eV, which belong to $Cu^{2+}$. Moreover, the presence of satellite peaks was attributed to Cu $2p_{3/2}$ and Cu $2p_{1/2}$ (Karikalan et al., 2017). There are no significant changes observed after the adsorption process, suggesting that adsorption of OTC did not change the chemical state of Cu in CuVA. However, effects can be observed for V 2p in Fig. 7(c) which shows that V 2p spectra of CuVA and CuVA R1 at 514.4 and 521.4 eV were associated with V $2p_{3/2}$ and V $2p_{1/2}$, respectively. This indicates that V exists in $V^{5+}$ state for the case of CuVA (Yamuna et al., 2021). After adsorption process, the V $2p_{3/2}$ and V $2p_{1/2}$ is shifted ~ 2 eV to higher binding energies. This suggests that adsorption of OTC changed the oxidation state of V.

# Investigation of Photocatalytic Properties

To validate that the increased removal of OTC in the presence of light was attributed to thermal effects rather than the photocatalytic properties of CuVA, photocatalytic degradation of MB dye was performed using the similar setup. 10 mg/L of MB dye was chosen as it is a well-studied pollutant for photocatalysis (Khalid et al., 2019) compared to OTC. MB dye was stirred in the dark overnight to achieve complete adsorption-desorption equilibrium prior to photocatalytic degradation to isolate the removal performance of adsorption and photocatalysis mechanisms (Huang et al., 2020). OTC on the other hand was impossible to analyze with this setup as there is no further change in removal efficiency after immersing in the solution overnight (Fig. S2), further suggesting that the removal is adsorption dominated. As shown in Fig. 7(d), the concentration of MB remained relatively unchanged after stirring overnight which indicated adsorption-desorption equilibrium have been achieved. Upon exposing to visible light for 3 h, it was observed that g-$C_3N_4$ performed the best, removing around 60% of MB. CuVA on the other hand shows practically zero improvement compared with the blank, suggesting that CuVA did not display photocatalytic behavior for MB degradation. However, CuVA/g-$C_3N_4$ composites such as C10, C30, and C50 exhibited a better photocatalytic efficiency compared to CuVA alone, owing to the photocatalytic behavior of g-$C_3N_4$. This further supports the claim from Tauc plot analysis (Fig. 4) that combining both CuVA and g-$C_3N_4$ did not yield a better performing heterojunction photocatalyst.

# Adsorption Performance of CuVA (pH and Temperature Dependence)

Figure 8(a) and (b) show that CuVA was unable to maintain its solid form and dissolved into the solution when the pH decreases below 3. Thus, removal performance of CuVA at pH 2.0 was not presented in Fig. 8(b). OTC was relatively stable throughout the pH range, only self-degraded by maximum of 10% after exposing to visible light for 6 h. By introducing CuVA into the solution, pH 11.0 performed the worst among the setup, only lowering to 50% of the initial concentration after 6 h. pH 8.5 and pH 5.0 performed relatively identical, at close to 90% removal after 6 h. Poor performance at pH 11.0 could be due to the surface of CuVA was negatively charged, resulting in the repulsion between the pollutant molecule ($OTC^{2-}$) and CuVA. As the pH lowered to 8.5 and 5.0, the OTC species shifted to a more positively charged species ($OTCH^-$ and $OTCH_2^{0(+/-)}$) (Ferchichi et al., 2022). Through this analysis, since pH 5.0 and 8.5 performed similarly, it was concluded that pH 5.0 is the optimum pH in this setup as it was closer to the initial condition of the solution before pH adjustment, at around 3.8. The thermodynamic of adsorption mechanism is shown in Fig. 8(c). OTC is stable even after exposing to 42°C for 6 h. By increasing the temperature, the adsorption performance of CuVA increased, up to 90% removal at 42°C with initial concentration of 100 mg/L. Performance at temperature of 37°C and 42°C were nearly identical (Fig. 8(d)) because CuVA has achieved adsorption-desorption equilibrium at 37°C. Further increase in temperature did not affect the final concentration of OTC after 6 h even though the initial kinetic of 42°C was higher.

# Adsorption Kinetic, Isotherms and Thermodynamics

Different kinetic models were fitted to identify the most suitable model and their model is expressed by equations provided in *Supplementary Information*. The models were fitted and shown in Fig. 9(a). Apart from intra-particle diffusion (IPD) model, the correlation coefficient ($R^2$) of other models was relatively similar in the high 0.99 region. For this reason, another statistical test method was employed to identify the best fitting model, chi-square ($\chi^2$). Table S2 summarizes their respective $R^2$ and $\chi^2$. Based on the fitted model, pseudo second-order (PSO) is the most suitable model with the highest $R^2$ and lowest $\chi^2$ to describe the adsorption mechanism. Table S3 lists the PSO rate of reaction at various temperature point using CuVA as adsorbent by fixing the equilibrium adsorption capacity at 180 mg/g. It can be observed that as temperature increased, the PSO rate of reaction increased. Based on collision theory, as temperature increased, the average kinetic energy of the molecules in the system will increase, this leads to higher collision probability between molecules and are more often able to reach the activation energy required for reaction (Fang et al., 2020).

In order to have insights into the mechanism of the adsorption process, isotherm models consist of one-, two- and three-parameter were selected to evaluate the experimental data (see *Supplementary Information*). The most direct method to solve the isotherm model is to transform all the equations into linear form to allow the constant to be calculated through linear regression. However, several studies had determined that linearization of isotherm model often produce statistical biases i.e., poor linearity despite high $R^2$ (González-Lópeza et al., 2022). Therefore, non-linear model was used to assess the parameters of the adsorption model. Similarly, both $R^2$ and $\chi^2$ were utilized as statistical test method. Table S4 presents the fittingness of all the isotherm model used and Fig. 9(b) shows the fitted model in a plot. Based on ranking model analysis, the two-parameter, Dubinnin-Radushkevich (D-R) model represented the most suitable model for the adsorption of OTC using CuVA with the highest $R^2$ and the lowest $\chi^2$. D-R isotherm model assumes the adsorbent size is comparable to micropore size. It assumes a Gaussian-type distribution onto heterogeneous surface (Wjihi et al., 2021). From the $K_{DR}$ obtained, the apparent adsorption energy, E (kJ/mol) can be determined using Eq. 6:

$$E = \frac{1}{\sqrt{2K_{DR}}} \quad (6)$$

According to D-R model, if E < 8 kJ/mol, the reaction is physisorption dominated, if E > 16 kJ/mol, the reaction is chemisorption dominated, if 8 < E < 16 kJ/mol, ion exchange dominates the reaction (Tsamo et al., 2019). By fitting the present work with D-R model, $q_m$ =3578.45 mg/g and $K_{DR}$ =0.00608 $mol^2 \cdot kJ^{-2}$ were obtained. Using this data, E = 9.07 kJ/mol was obtained, and therefore the adsorption mechanism was ion-exchange dominated.

The thermodynamic properties of the adsorption reaction were calculated using Arrhenius's equation (see *Supplementary Information*). Figure 9(c) shows the non-linear fitting of Arrhenius's equation, $E_a$ was

calculated to be 134.87 kJ/mol and A of 1.20 x $10^{22}$ g·$mg^{-1}$·$min^{-1}$ was obtained. Activation energy plays a crucial role in governing the reaction rate. At a specific temperature, a higher activation energy leads to a slower reaction, whereas a lower activation energy results in a faster reaction. At room temperature, if the calculated activation energy is below 40 kJ/mol, the reaction proceeds rapidly; however, if it exceeds 120 kJ/mol, the reaction rate proceeds rather slowly. For ion exchange of OTC on CuVA, the apparent activation energy of PSO kinetic model is 134.87 kJ/mol, this shows that the adsorption process is slow. To understand the change in enthalpy and entropy of the adsorption reaction, Gibbs free energy, $\Delta_r G$ was calculated using Van't-Hoff equation (see *Supplementary Information).* As shown in Fig. 9(d), the fitted $\Delta_r S$ was calculated as 244.61 J·$mol^{-1}$·$K^{-1}$ and the $\Delta_r H$ was calculated as 71.06 kJ·$mol^{-1}$. Since $\Delta_r H$ is positive, the adsorption process was endothermic and at the same instance, positive $\Delta_r S$ indicates the adsorption process was becoming more irreversible as temperature increased (Meloun et al., 2020). From the Table S5, it can be concluded that the adsorption reaction was spontaneous when the temperature was higher than 290.5 K (17.35°C), and the reaction became more favorable as temperature increased.

# Reusability of CuVA

Life cycle assessment were carried out (Fig. 10 (a)) to determine the lifetime of CuVA as an adsorbent. It was found that after 5 cycles, the sample was still able to remove 46.93% of the pollutant after 6 h, without any desorption step in between. By considering adsorbed mass of OTC in loading after each adsorption cycle, the apparent adsorption capacity was readjusted using Eq. 7, and the values appears to be remained unchanged (Table S6).

$$q_{e,adjusted} = \frac{(C_0 - C_e)\,V}{(m - m_{OTC})} \quad (7)$$

where m is the mass of CuVA used and $m_{OTC}$ is the mass of OTC being adsorbed previously by the CuVA.

The FTIR spectra of the recycled sample (Fig. 10(b)) indicates that with each successive cycle, the spectra increasingly exhibited similarities to the spectrum of OTC. This observation further reinforces the notion that the dominant removal mechanism was adsorption, and there was no evidence of any additional decomposition reactions taking place.

# Conclusions

Different weight percentage of CuVA (10, 30 and 50 wt%) was successfully incorporated onto g-$C_3N_4$ using wet chemical method. These weightages were verified using EDX, XRD and FTIR, with all three of the characterization techniques showing positive trends. The prepared composites were direct bandgap in nature and the bandgap decreased as the weightage of CuVA increased, down from 3.05 to 2.47 eV. The enhancement of OTC removal was not significantly influenced by the photocatalytic characteristics of g-$C_3N_4$ as the contribution to the decrease in OTC concentration was minor (10% removal compared to

80% removal by CuVA). Increased removal of OTC noted under light conditions was attributed to thermal effects rather than the photocatalytic properties of CuVA. The adsorption of OTC using CuVA has demonstrated high effectiveness, with up to 90% of OTC being removed under optimized conditions at 42°C and pH 5.0 within 3 h. Adsorption kinetics and isotherms model of CuVA resembled more to pseudo-second order model and D-R model the most, respectively. Based on the fitted parameters, E = 9.07 kJ/mol was obtained which indicated the adsorption mechanism was predominantly influenced by ion-exchange. Both of thermodynamic and Gibb's free energy analysis performed on CuVA showed the adsorption behavior was slow in nature and endothermic ($\Delta_r H$ = 71.06 kJ/mol). The adsorption reaction was more irreversible as temperature increased ($\Delta_r S$ = 244.61 $J{\cdot}mol^{-1}{\cdot}K^{-1}$) and it can be initiated from 17.35°C and above.

# Declarations

### Ethical Approval

Not applicable

### Consent to Participate

Not applicable

### Consent to Publish

Not applicable

### Author Contributions

Wei Qing Wee and Lan Ching Sim contributed to the study conception and design. Material preparation, data collection and analysis were performed by Wei Qing Wee and Lan Ching Sim. The first draft of the manuscript was written by Wei Qing Wee. Kah Hon Leong and Azrina Abdul Aziz validated the results and provided the resources to conduct research work. All authors commented on previous versions of the manuscript. All authors read and approved the final manuscript.

### Funding

The research has been carried out under Fundamental Research Grant Scheme project FRGS/1/2023/TK08/UTAR/02/8 provided by Ministry of Higher Education of Malaysia.

### Competing Interests

The authors have no relevant financial or non-financial interests to disclose

# References

1. Amrute AP, De Bellis J, Felderhoff M, Schüth F (2021) Mechanochemical synthesis of catalytic materials. Chem Eur J 27(23):6819-6847. https://doi.org/10.1002/chem.202004583
2. Baudys M, Paušová Š, Praus P, Brezová V, Dvoranová D, Barbieriková Z, Krýsa J (2020) Graphitic carbon nitride for photocatalytic air treatment. Mater 13(13):3038. https://doi.org/10.3390/ma13133038
3. Bayat A, Mahjoub AR, Amini MM (2018) Facile hydrothermal synthesis of the colloidal hierarchical Volborthite ($Cu_3V_2O_7(OH)_2.2H_2O$) hollow sphere phosphors. J Lumin 204:382-385. https://doi.org/10.1016/j.jlumin.2018.07.046
4. Benisti I, Shaik F, Xing Z, Ben-refael A, Amirav L, Paz Y (2021) The effect of Pt cocatalyst on the performance and transient IR spectrum of photocatalytic g-$C_3N_4$ nanospheres. Appl Surf Sci 542:148432. https://doi.org/10.1016/j.apsusc.2020.148432
5. Chairungsri W, Subkomkaew A, Kijjanapanich P, Chimupala Y (2022) Direct dye wastewater photocatalysis using immobilized titanium dioxide on fixed substrate. Chemosphere 286:131762. https://doi.org/10.1016/j.chemosphere.2021.131762
6. Chen K, Zhang T, Chen X, He Y, Liang X (2018) Model construction of micro-pores in shale: A case study of Silurian Longmaxi Formation shale in Dianqianbei area, SW China. Pet Explor Dev 45(3):412-421. https://doi.org/10.1016/S1876-3804(18)30046-6
7. Chen X, Yu F, Gong F, Li Y (2023) Preparation of 3D porous $CeO_2$/g-$C_3N_4$ photocatalyst via facile one–step calcination for rapid removing of tetracycline. Vacuum 213:112090. https://doi.org/10.1016/j.vacuum.2023.112090
8. Cheng X, Guan R, Chen Y, Qian Y, Shang Q, Sun Y (2023) Adsorption and photocatalytic degradation process of oxytetracycline using mesoporous Fe-$TiO_2$ based on high-resolution mass spectrometry. Chem Eng J 460:141618. https://doi.org/10.1016/j.cej.2023.141618
9. Chin JY, Ahmad AL, Low SC (2023) Antibiotics oxytetracycline removal by photocatalyst titanium dioxide and graphitic carbon nitride in aquaculture wastewater. J Environ Manage 343:118231. https://doi.org/10.1016/j.jenvman.2023.118231
10. Fang D, Zhuang X, Huang L, Zhang Q, Shen Q, Jiang L, Xu X, Ji F (2020) Developing the new kinetics model based on the adsorption process: From fitting to comparison and prediction. Sci Total Environ 725:138490. https://doi.org/10.1016/j.scitotenv.2020.138490
11. Fawzy SM, Omar MM, Allam NK (2019) Photoelectrochemical water splitting by defects in nanostructured multinary transition metal oxides. Sol Energy Mater Sol Cells 194:184-194. https://doi.org/10.1016/j.solmat.2019.02.011
12. Feng D, Cheng Y, He J, Zheng L, Shao D, Wang W, Wang W, Lu F, Dong H, Liu H, Zheng R, Liu H (2017) Enhanced photocatalytic activities of g-$C_3N_4$ with large specific surface area via a facile one-step synthesis process. Carbon 125:454-463. https://doi.org/10.1016/j.carbon.2017.09.084
13. Ferchichi K, Amdouni N, Chevalier Y, Hbaieb S (2022) Low-cost Posidonia oceanica bio-adsorbent for efficient removal of antibiotic oxytetracycline from water. Environ Sci Pollut Res 29(55):83112-

83125. https://doi.org/10.1007/s11356-022-21647-3

14. Ge F, Huang S, Yan J, Jing L, Chen F, Xie M, Xu Y, Xu H, Li H (2021) Sulfur promoted n-π* electron transitions in thiophene-doped g-$C_3N_4$ for enhanced photocatalytic activity. Chinese J Catal 42(3):450-459. https://doi.org/10.1016/S1872-2067(20)63674-9
15. Giannakopoulou T, Papailias I, Todorova N, Boukos N, Liu Y, Yu J, Trapalis C (2017) Tailoring the energy band gap and edges' potentials of g-$C_3N_4$/$TiO_2$ composite photocatalysts for $NO_x$ removal. Chem Eng J 310:571-580. https://doi.org/10.1016/j.cej.2015.12.102
16. González-López ME, Laureano-Anzaldo CM, Pérez-Fonseca AA, Arellano M, Robledo-Ortíz JR (2022) A critical overview of adsorption models linearization: methodological and statistical inconsistencies. Sep Purif Rev 51(3):358-372. https://doi.org/10.1080/15422119.2021.1951757
17. Hak CH, Leong KH, Chin YH, Saravanan P, Tan ST, Chong WC, Sim LC (2020) Water hyacinth derived carbon quantum dots and g-$C_3N_4$ composites for sunlight driven photodegradation of 2, 4-dichlorophenol. SN Appl Sci 2:1-4. https://doi.org/10.1007/s42452-020-2840-y
18. Hiroi Z, Ishikawa H, Yoshida H, Yamaura JI, Okamoto Y (2019) Orbital transitions and frustrated magnetism in the kagome-type copper mineral volborthite. Inorg Chem 58(18):11949-11960. https://doi.org/10.1021/acs.inorgchem.9b01165
19. Huang S, Wang G, Liu J, Du C, Su Y (2020) A novel $CuBi_2O_4$/BiOBr direct Z-scheme photocatalyst for efficient antibiotics removal: synergy of adsorption and photocatalysis on degradation kinetics and mechanism insight. ChemCatChem 12(17):4431-4445. https://doi.org/10.1002/cctc.202000634
20. Isari AA, Mehregan M, Mehregan S, Hayati F, Kalantary RR, Kakavandi B (2020) Sono-photocatalytic degradation of tetracycline and pharmaceutical wastewater using $WO_3$/CNT heterojunction nanocomposite under US and visible light irradiations: a novel hybrid system. J Hazard Mater 390:122050. https://doi.org/10.1016/j.jhazmat.2020.122050
21. Jain S, Sharma B, Thakur N, Mishra S, Sarma TK (2020) Copper pyrovanadate nanoribbons as efficient multienzyme mimicking nanozyme for biosensing applications. ACS Appl Nano Mater 3(8):7917-7929. https://doi.org/10.1021/acsanm.0c01415
22. Jiang W, Luo W, Zong R, Yao W, Li Z, Zhu Y (2016) Polyaniline/carbon nitride nanosheets composite hydrogel: a separation-free and high-efficient photocatalyst with 3D hierarchical structure. Small 12(32):4370-4378. https://doi.org/10.1002/smll.201601546
23. Kamble GS, Ling YC (2020) Solvothermal synthesis of facet-dependent $BiVO_4$ photocatalyst with enhanced visible-light-driven photocatalytic degradation of organic pollutant: assessment of toxicity by zebrafish embryo. Sci Rep 10(1):12993. https://doi.org/10.1038/s41598-020-69706-4
24. Karikalan N, Karthik R, Chen SM, Karuppiah C, Elangovan A (2017) Sonochemical synthesis of sulfur doped reduced graphene oxide supported CuS nanoparticles for the non-enzymatic glucose sensor applications. Sci Rep 7(1):2494. https://doi.org/10.1038/s41598-017-02479-5
25. Khalid NR, Hammad A, Tahir MB, Rafique M, Iqbal T, Nabi G, Hussain MK (2019) Enhanced photocatalytic activity of Al and Fe co-doped ZnO nanorods for methylene blue degradation. Ceram

Int 45(17):21430-21435. https://doi.org/10.1016/j.ceramint.2019.07.132

26. Khan I, Qurashi A (2017) Shape controlled synthesis of copper vanadate platelet nanostructures, their optical band edges, and solar-driven water splitting properties. Sci Rep 7(1):14370. https://doi.org/10.1038/s41598-017-14111-7
27. Kraemer SA, Ramachandran A, Perron GG (2019) Antibiotic pollution in the environment: from microbial ecology to public policy. Microorganisms 7(6):180. https://doi.org/10.3390/microorganisms7060180
28. Li S, Cui J, Wu X, Zhang X, Hu Q, Hou X (2019) Rapid in situ microwave synthesis of $Fe_3O_4$@ MIL-100 (Fe) for aqueous diclofenac sodium removal through integrated adsorption and photodegradation. J Hazard Mater 373:408-416. https://doi.org/10.1016/j.jhazmat.2019.03.102
29. Liang Y, Liu P, Li HB, Yang GW (2012) Synthesis and characterization of copper vanadate nanostructures *via* electrochemistry assisted laser ablation in liquid and the optical multi-absorptions performance. CrystEngComm 14(9):3291-3296. https://doi.org/10.1039/C2CE06347F
30. Lin X, Xu Q, Gan L, Owens G, Chen Z (2022) Cyclodextrin modified green synthesized graphene oxide@ iron nanoparticle composites for enhanced removal of oxytetracycline. J Colloid Interface Sci 608:3159-3167. https://doi.org/10.1016/j.jcis.2021.11.049
31. Long R, Yu Z, Tan Q, Feng X, Zhu X, Li X, Wang P (2021) $Ti_3C_2$ MXene/$NH_2$-MIL-88B (Fe): Research on the adsorption kinetics and photocatalytic performance of an efficient integrated photocatalytic adsorbent. Appl Surf Sci 570:151244. https://doi.org/10.1016/j.apsusc.2021.151244
32. Meloun M, Pfeiferová A, Javůrek M, Pekárek T (2020) Determination of acid dissociation constants, enthalpy, entropy and Gibbs free energy of the baricitinib by the UV-metric and pH-metric analysis. J Pharm Biomed Anal 191:113532. https://doi.org/10.1016/j.jpba.2020.113532
33. Modwi A, Basith NM, Ghoniem MG, Ismail M, Ben Aissa MA, Khezami L, Bououdina M (2023) Efficient Pb (II) adsorption in aqueous solution by hierarchical 3D/2D $TiO_2$/CNNS nanocomposite. Mater Sci Eng B 289:116191. https://doi.org/10.1016/j.mseb.2022.116191
34. Mog M, Ngasotter S, Tesia S, Waikhom D, Panda SP, Sharma S, Varshney S (2020) Problems of antibiotic resistance associated with oxytetracycline use in aquaculture: A review. J Entomol Zool Stud 8:1075-1082.
35. Nagappagari LR, Lee J, Lee H, Jeong B, Lee K (2021) Energy and environmental applications of $Sn^{4+}$/$Ti^{4+}$ doped α-$Fe_2O_3$@$Cu_2O$/CuO photoanode under optimized photoelectrochemical conditions. Environ Pollut 271:116318. https://doi.org/10.1016/j.envpol.2020.116318
36. Nguyen Van M, Mai OLT, Pham Do C, Lam Thi H, Pham Manh C, Nguyen Manh H, Pham Thi D, Do Danh B (2020) Fe-doped g-$C_3N_4$: High-performance photocatalysts in rhodamine B decomposition. Polymers 12(9):1963. https://doi.org/10.3390/polym12091963
37. Pareek S, Sharma M, Lal S, Quamara JK (2018) Polymeric graphitic carbon nitride–barium titanate nanocomposites with different content ratios: a comparative investigation on dielectric and optical properties. J Mater Sci: Mater Electron 29:13043-13051. https://doi.org/10.1007/s10854-018-9426-0

38. Sánchez-Loredo MG, Palomares-Sánchez SA, Labrada-Delgado GJ, Helbig T, Chekhonin P, Ebert D, Möckel R, Afriyie JO, Kelly N (2023) Preparation of volborthite by a facile synthetic chemical solvent extraction method. Nanomater 13(13):1977. https://doi.org/10.3390/nano13131977
39. Senasu T, Lorwanishpaisarn N, Hemavibool K, Nijpanich S, Chanlek N, Nanan S (2023) Construction of g-$C_3N_4$/BiOCl/CdS heterostructure photocatalyst for complete removal of oxytetracycline antibiotic in wastewater. Sep Purif Technol 306:122735. https://doi.org/10.1016/j.seppur.2022.122735
40. Song A, Liu S, Wang Q, Gao D, Hu J (2023) Comprehensive evaluation of copper vanadate (α-$CuV_2O_6$) for use as a photoanode material for photoelectrochemical water splitting. J Environ Chem Eng 11(3):109892. https://doi.org/10.1016/j.jece.2023.109892
41. Song Y, Zhao X, Feng X, Chen L, Yuan T, Zhang F (2022) Z-scheme $Cu_2O$/Cu/$Cu_3V_2O_7(OH)_2.2H_2O$ heterostructures for efficient visible-light photocatalytic $CO_2$ reduction. ACS Appl Energy Mater 5(9):10542-10552. https://doi.org/10.1021/acsaem.2c01252
42. Tan TL, Krusnamurthy PA, Nakajima H, Rashid SA (2020) Adsorptive, kinetics and regeneration studies of fluoride removal from water using zirconium-based metal organic frameworks. RSC Adv 10(32):18740-18752. https://doi.org/10.1039/D0RA01268H
43. Thendral KT, Amutha M, Ragunathan R (2023) Design and development of copper cobaltite ($CuCo_2O_4$) nanoparticle for antibacterial anticancer and photocatalytic activity. Mater Lett 134720. https://doi.org/10.1016/j.matlet.2023.134720
44. Tsamo C, Paltahe A, Fotio D, Vincent TA, Sales WF (2019) One-, two-, and three-parameter isotherms, kinetics, and thermodynamic evaluation of Co (II) removal from aqueous solution using dead neem leaves. Int J Chem Eng 2019:1-4. https://doi.org/10.1155/2019/6452672
45. Vignesh S, Chandrasekaran S, Srinivasan M, Anbarasan R, Perumalsamy R, Arumugam E, Shkir M, Algarni H, AlFaify S (2022) $TiO_2$-$CeO_2$/g-$C_3N_4$ S-scheme heterostructure composite for enhanced photo-degradation and hydrogen evolution performance with combined experimental and DFT study. Chemosphere 288:132611. https://doi.org/10.1016/j.chemosphere.2021.132611
46. Wang P, Yang H, Wang D, Chen A, Dai WL, Zhao X, Yang J, Wang X (2018) Activation of Kagome lattice-structured $Cu_3V_2O_7(OH)_2.2H_2O$ volborthite via hydrothermal crystallization for boosting visible light-driven water oxidation. Phys Chem Chem Phys 20(38):24561-24569. https://doi.org/10.1039/C8CP03530J
47. Wjihi S, Aouaini F, Erto A, Balsamo M, Lamine AB (2021) Advanced interpretation of $CO_2$ adsorption thermodynamics onto porous solids by statistical physics formalism. Chem Eng J 406:126669. https://doi.org/10.1016/j.cej.2020.126669
48. Xie YC, Chen JH, Lin WY, Wu RJ, Fegade U, Patil N, Ansar S, Pandey S (2023) Triangular silver nanoplates-$BiVO_4$ composite for the photocatalytic $CO_2$ reduction under irradiating LED light source. Opt Mater 143:114141. https://doi.org/10.1016/j.optmat.2023.114141

49. Yamuna A, Chen TW, Chen SM, Jiang TY (2021) Facile synthesis of single-crystalline Fe-doped copper vanadate nanoparticles for the voltammetric monitoring of lethal hazardous fungicide carbendazim. Microchim Acta 188:1-2. https://doi.org/10.1007/s00604-021-04941-8
50. Ye MY, Zhao ZH, Hu ZF, Liu LQ, Ji HM, Shen ZR, Ma TY (2016) 0D/2D heterojunctions of vanadate quantum dots/graphitic carbon nitride nanosheets for enhanced visible-light-driven photocatalysis. Angew Chem Int Ed 56(29):8407-8411. https://doi.org/10.1002/anie.201611127
51. Yu Y, Huang H (2023) Coupled adsorption and photocatalysis of g-$C_3N_4$ based composites: Material synthesis, mechanism, and environmental applications. Chem Eng J 453:139755. https://doi.org/10.1016/j.cej.2022.139755
52. Yu Y, Xu W, Fang J, Chen D, Pan T, Feng W, Liang Y, Fang Z (2020) Soft-template assisted construction of superstructure $TiO_2$/$SiO_2$/g-$C_3N_4$ hybrid as efficient visible-light photocatalysts to degrade berberine in seawater via an adsorption-photocatalysis synergy and mechanism insight. Appl Catal B: Environ 268:118751. https://doi.org/10.1016/j.apcatb.2020.118751
53. Zequine C, Bhoyate S, Wang F, Li X, Siam K, Kahol PK, Gupta RK (2019) Effect of solvent for tailoring the nanomorphology of multinary $CuCo_2S_4$ for overall water splitting and energy storage. J Alloys Compd 784:1-7. https://doi.org/10.1016/j.jallcom.2019.01.012

# Figures

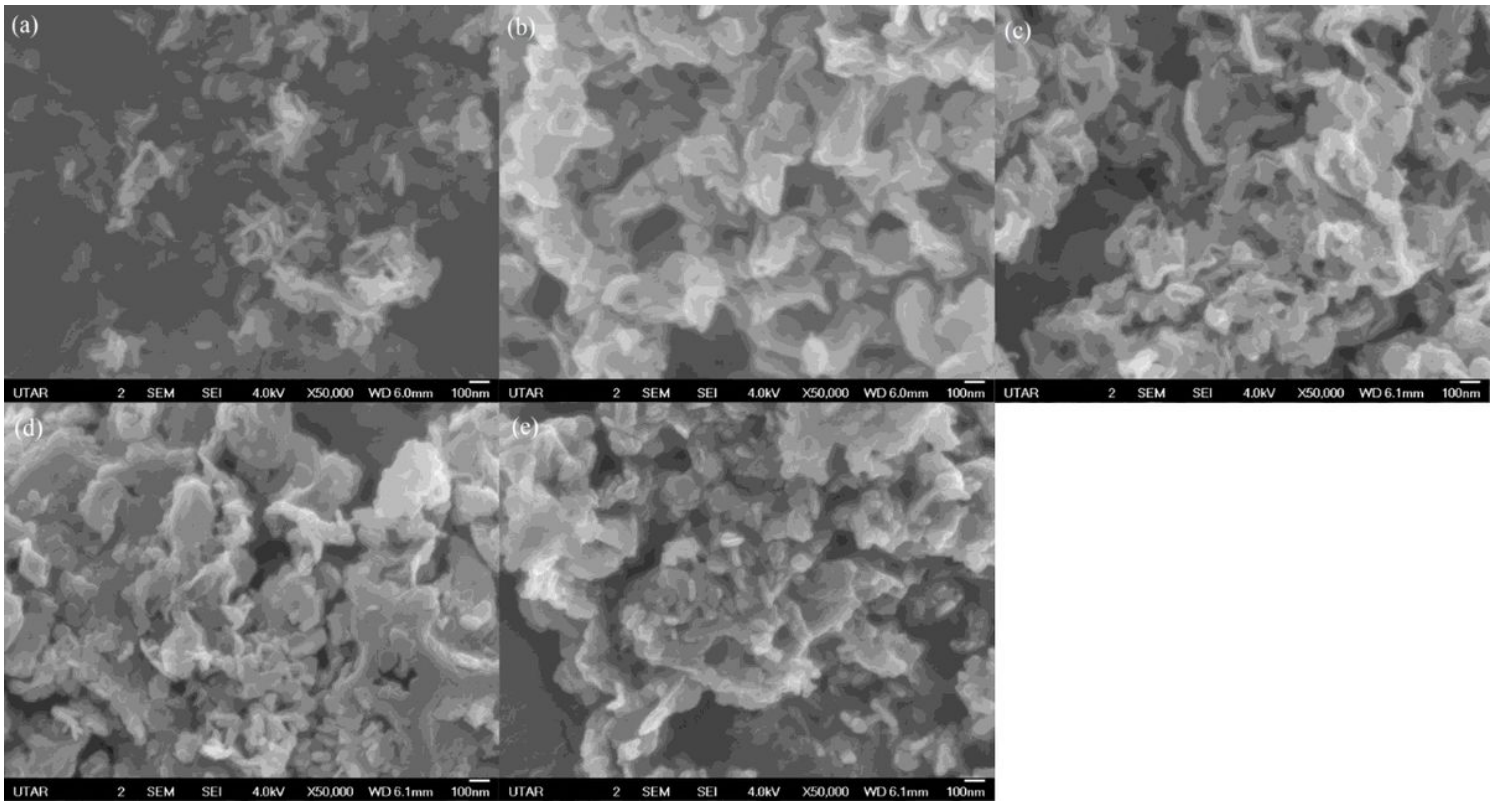


**Figure 1**

FESEM image of (a) CuVA, (b) g-$C_3N_4$, (c) C10, (d) C30 and (e) C50.

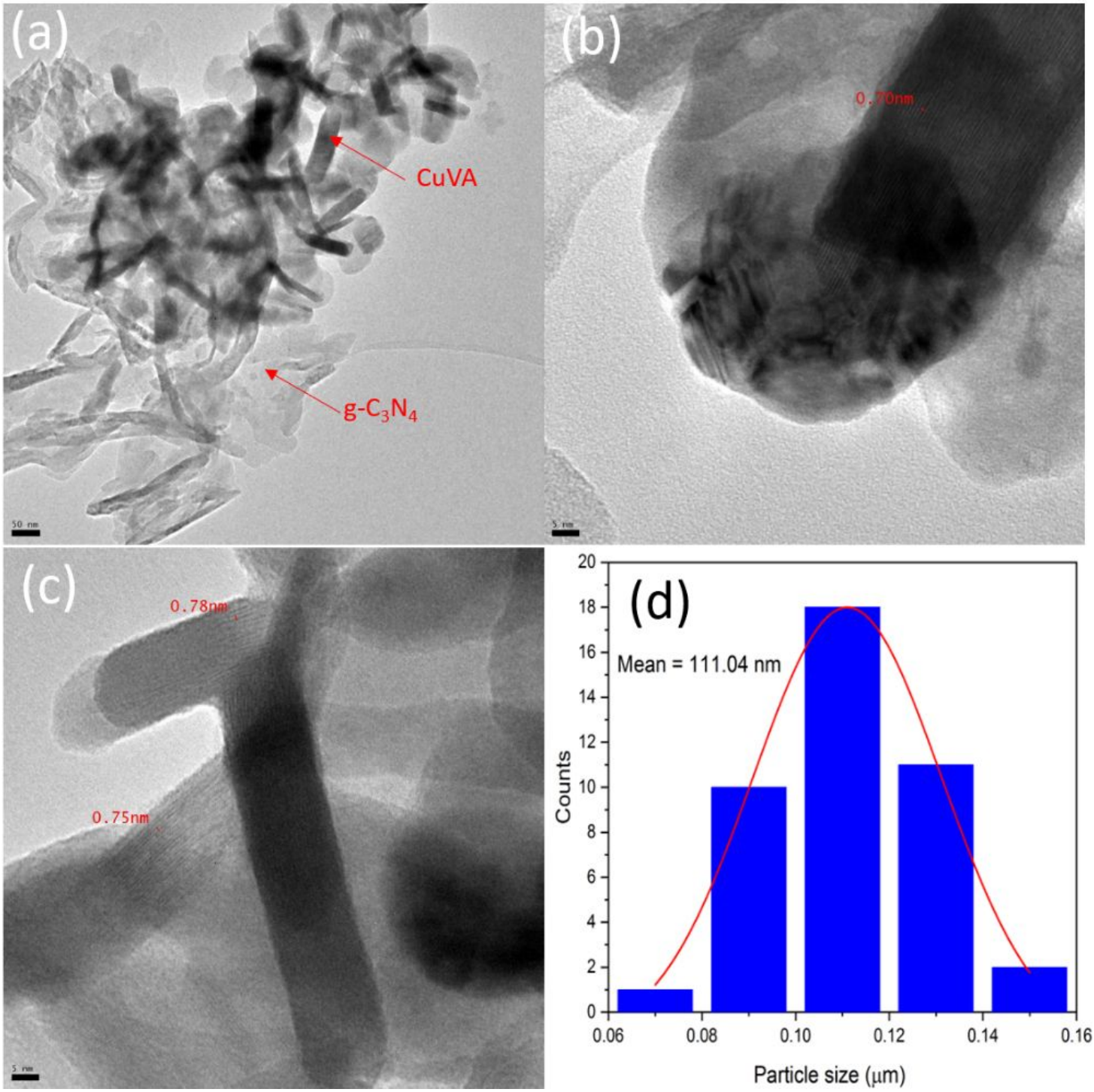


## Figure 2

(a) HRTEM image of C50, lattice fringes of (b) C50, (c) CuVA at 195k magnification, and (d) CuVA particle size distribution.

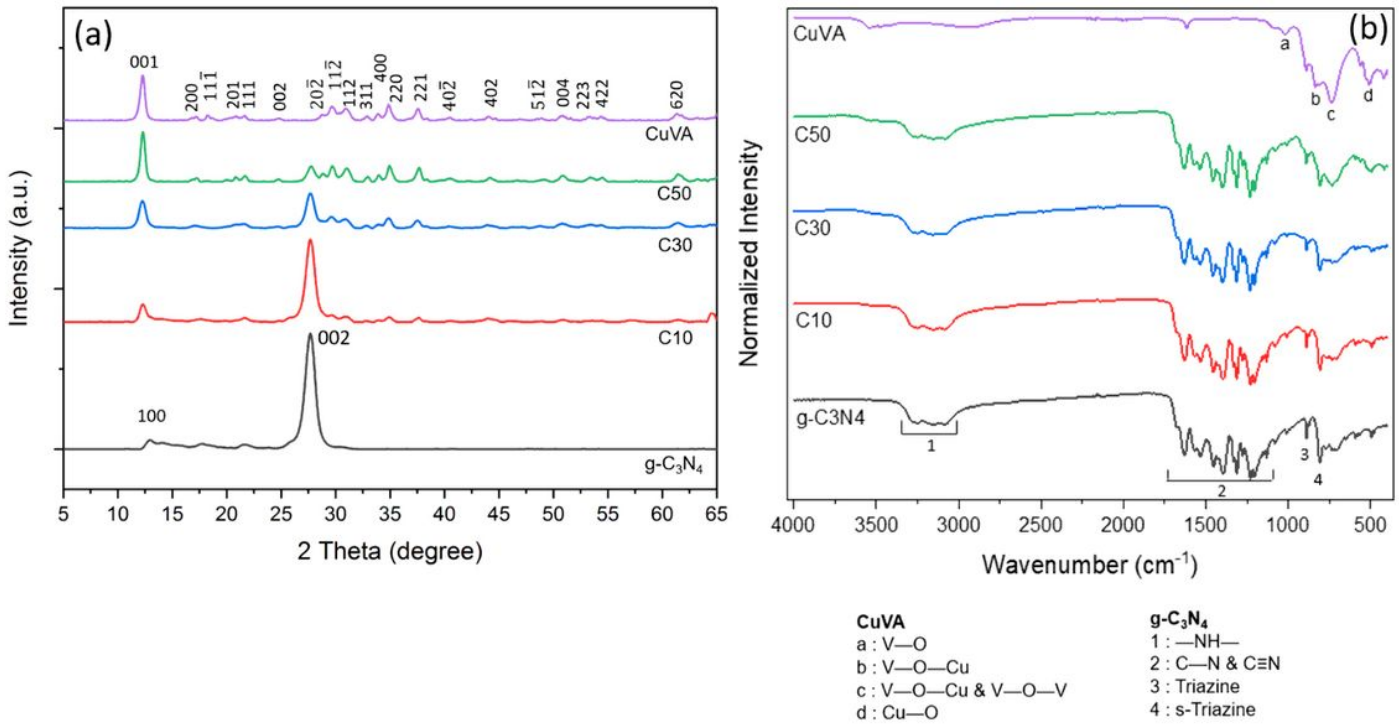


## Figure 3

(a) XRD pattern, and (b) FTIR spectra of g-$C_3N_4$, C10, C30, C50 and CuVA.

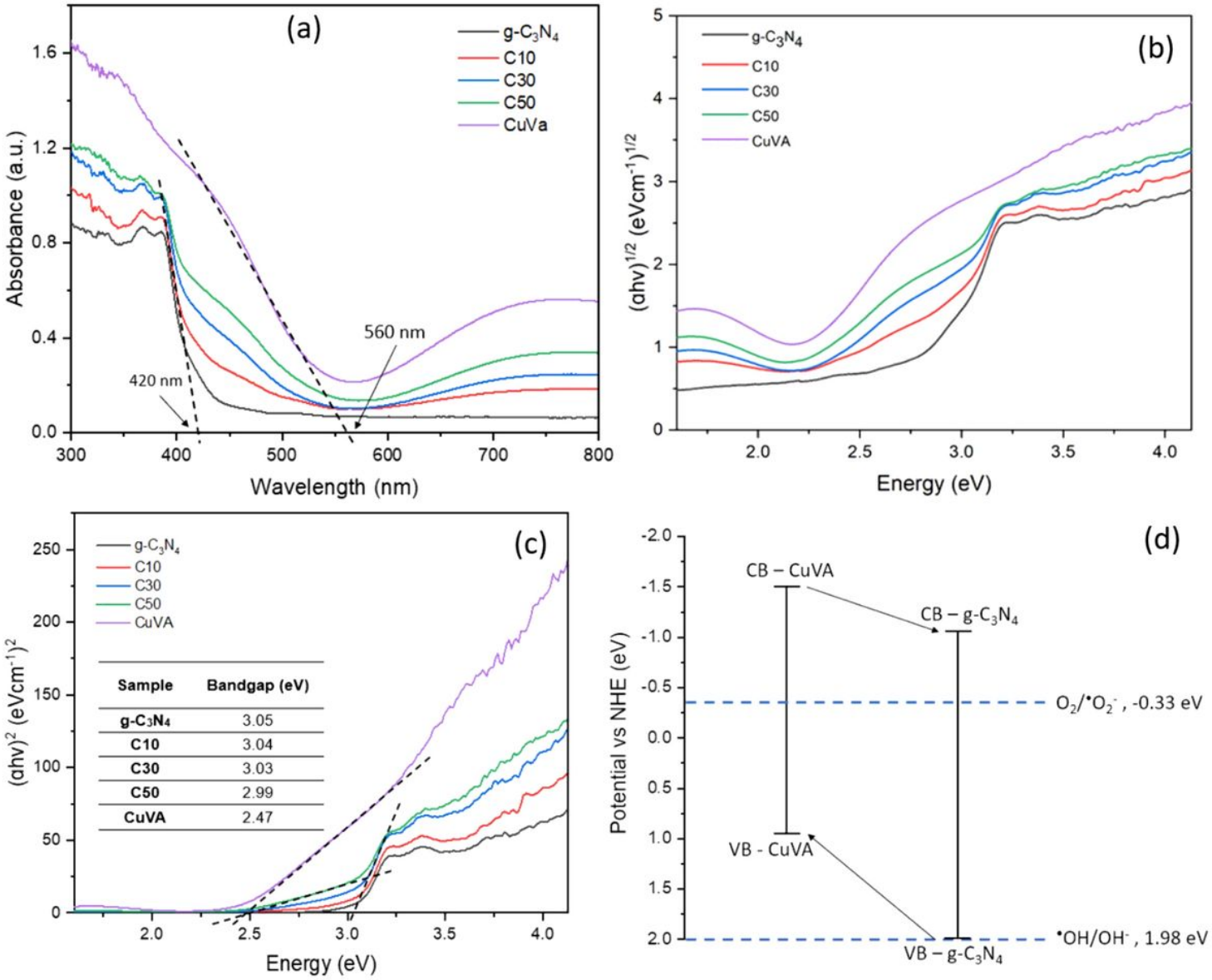


## Figure 4

(a) Kubelka–Munk transformation of UV-Vis DRS of as-prepared samples, Tauc plot using (b) indirect bandgap and (c) direct band gap calculated from Kubelka-Munk transformation. Inset table of (c) shows the band gap energy of the samples, and (d) Band-edge position of CuVA and g-$C_3N_4$.

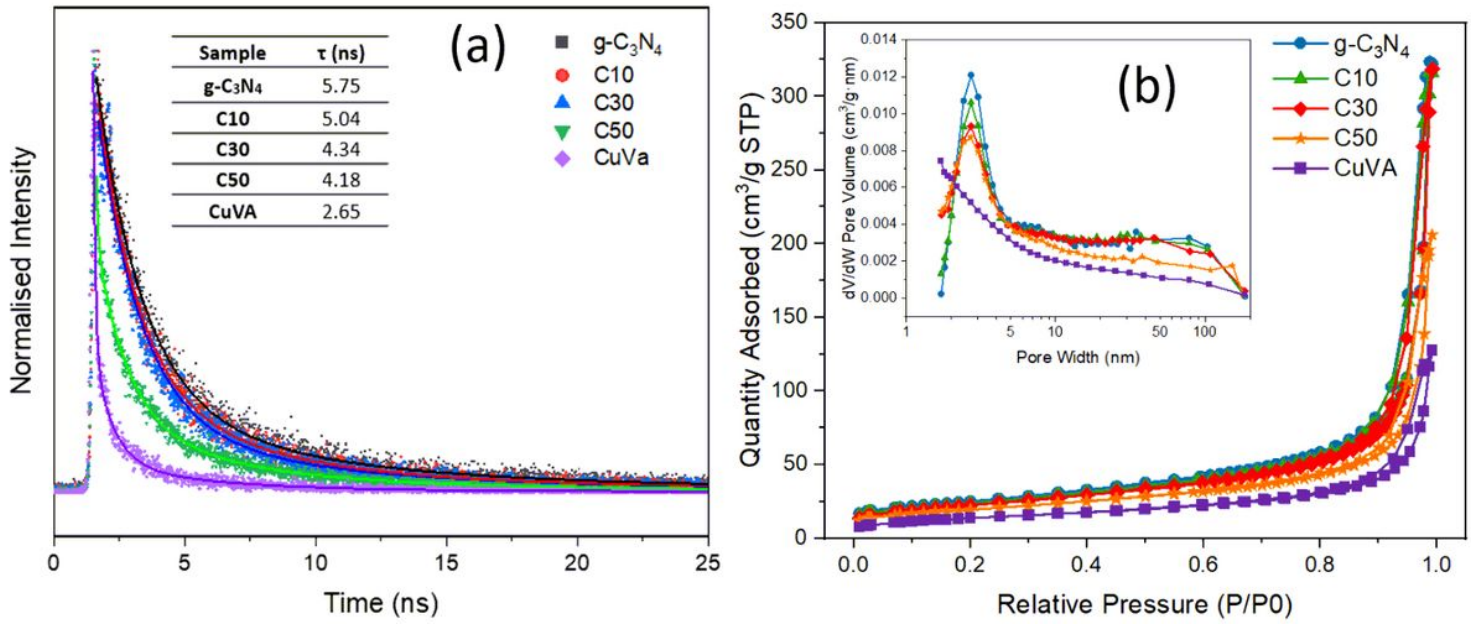


## Figure 5

(a) TRPL spectra, and (b) BET specific surface area of g-$C_3N_4$, C10, C30, C50 and CuVA. Inset table of (a) shows recombination time of all samples.

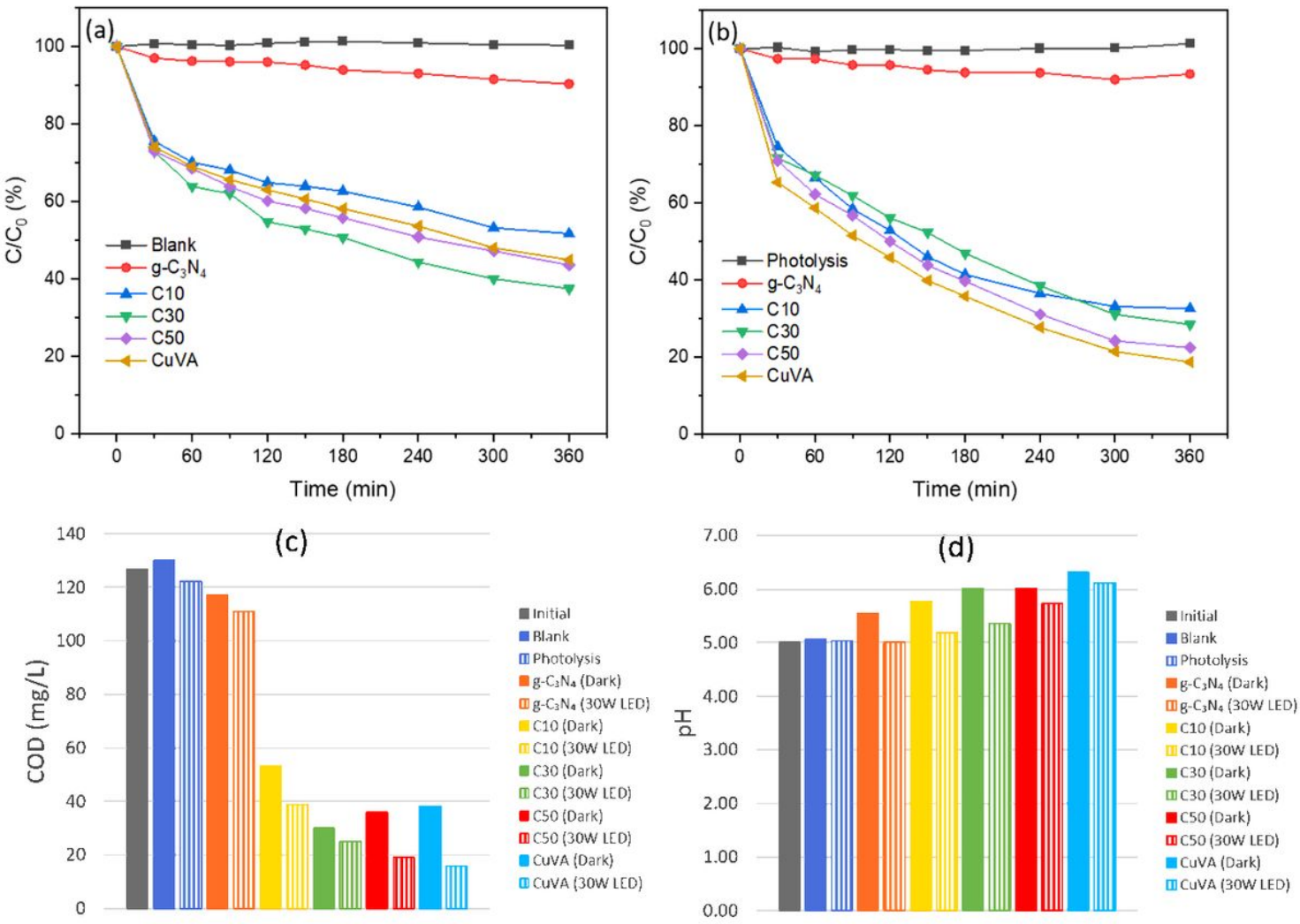


## Figure 6

OTC removal performance curves of the blank, g-$C_3N_4$, C10, C30, C50 and CuVA (a) in the absence of light (dark), (b) in the presence of light, (c) COD, and (d) pH of remaining OTC solution after removing OTC in the dark and light irradiation.

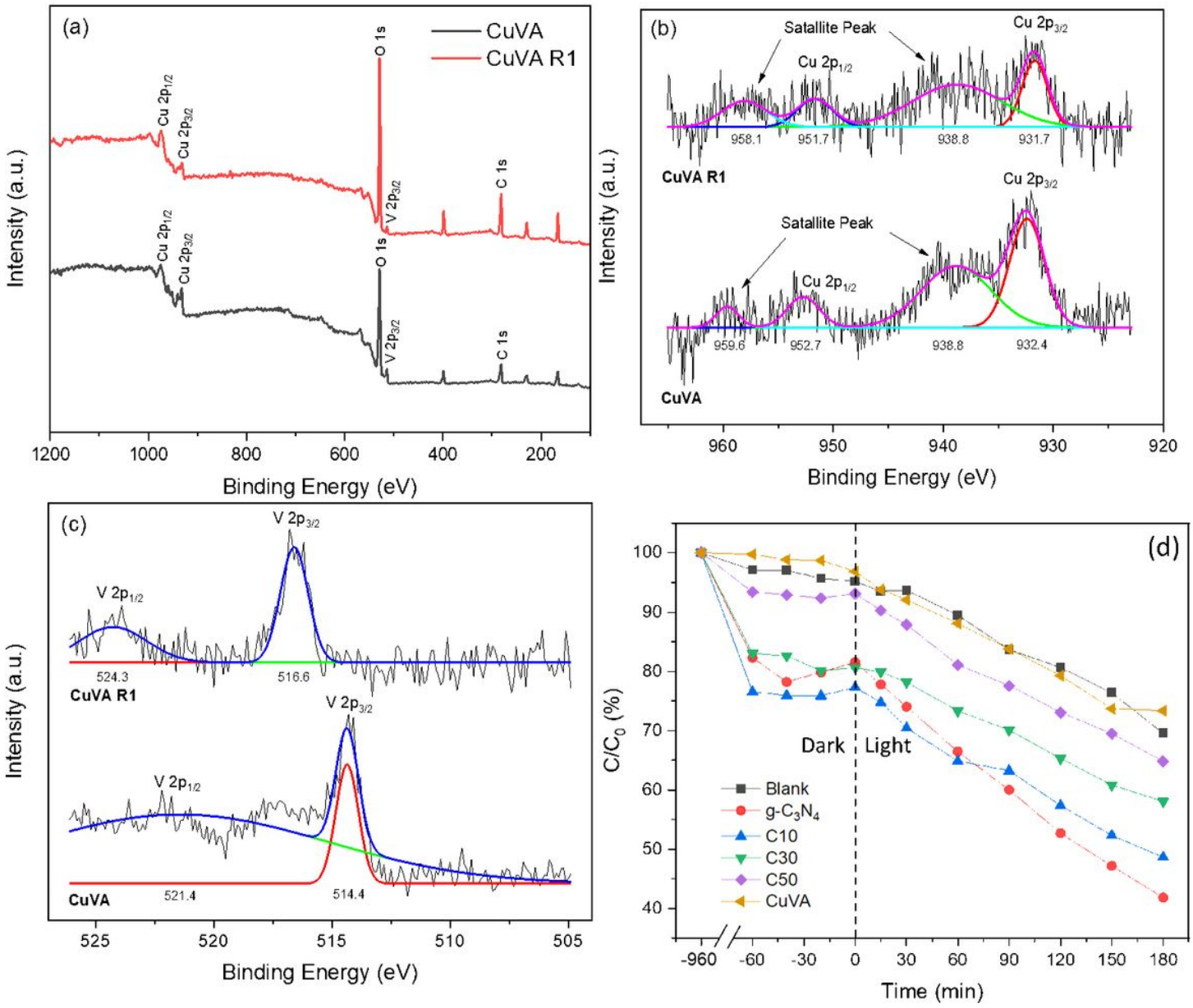


## Figure 7

(a) XPS survey of CuVA and CuVA R1 (spent CuVA). High magnified spectra of (b) Cu 2p, (c) V 2p, and (d) Photocatalytic performance of all samples for MB dye removal.

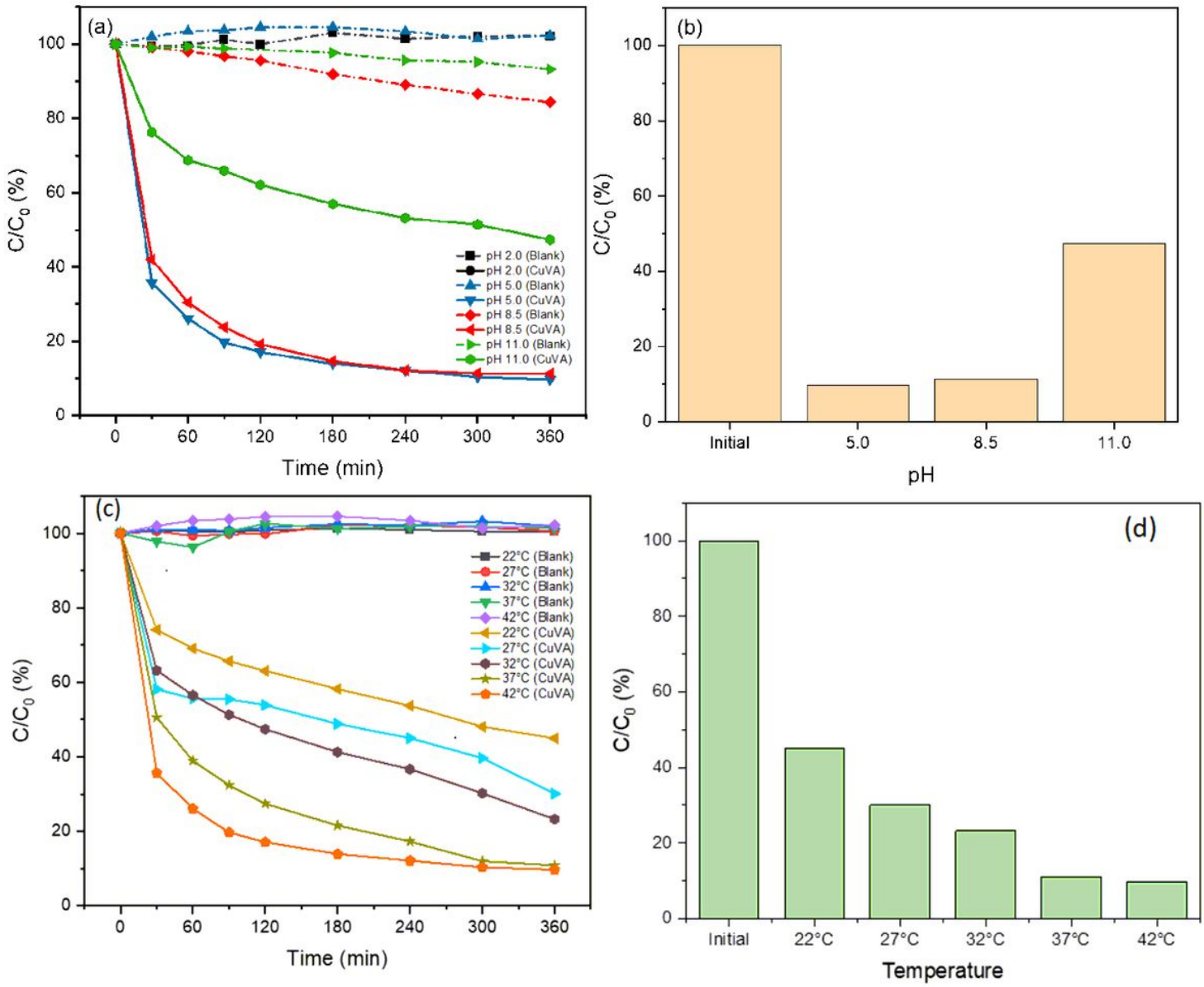


## Figure 8

Removal performance at various pH and fixed temperature setup of CuVA represented in (a) and (c) timeline, and (b) and (d) bar chart of $C/C_0$ at T = 360 mins at various pH and temperature.

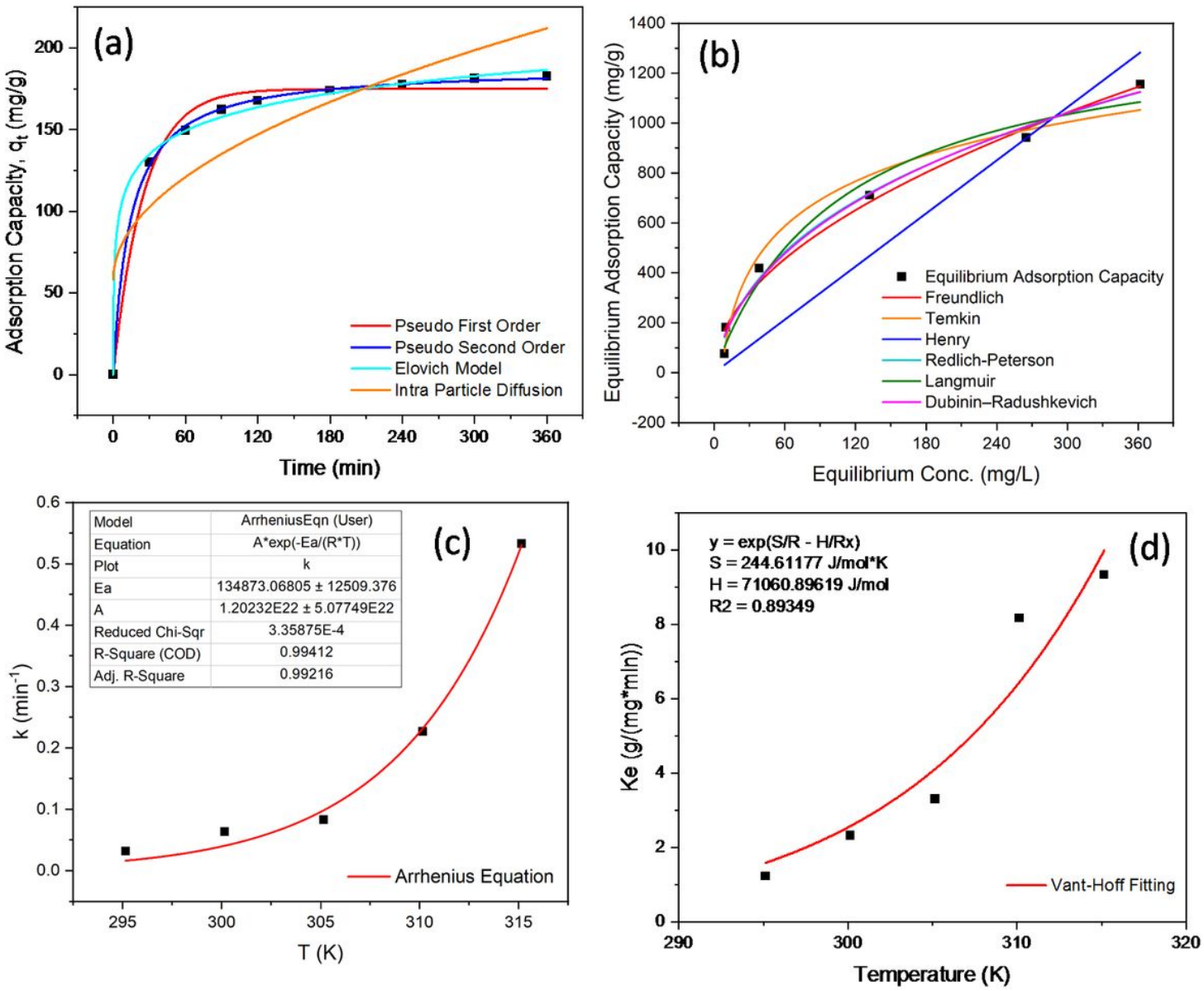


## Figure 9

(a) Non-linear kinetic models of removal of OTC using CuVA at 42 °C, (b) Fitting of the isotherm models on data from present work, (c) Arrhenius's equation using PSO rate of reaction obtained from fitting PSO kinetic models, and (d) Fitting of Van't-Hoff equation from temperature dependency study of CuVA towards OTC.

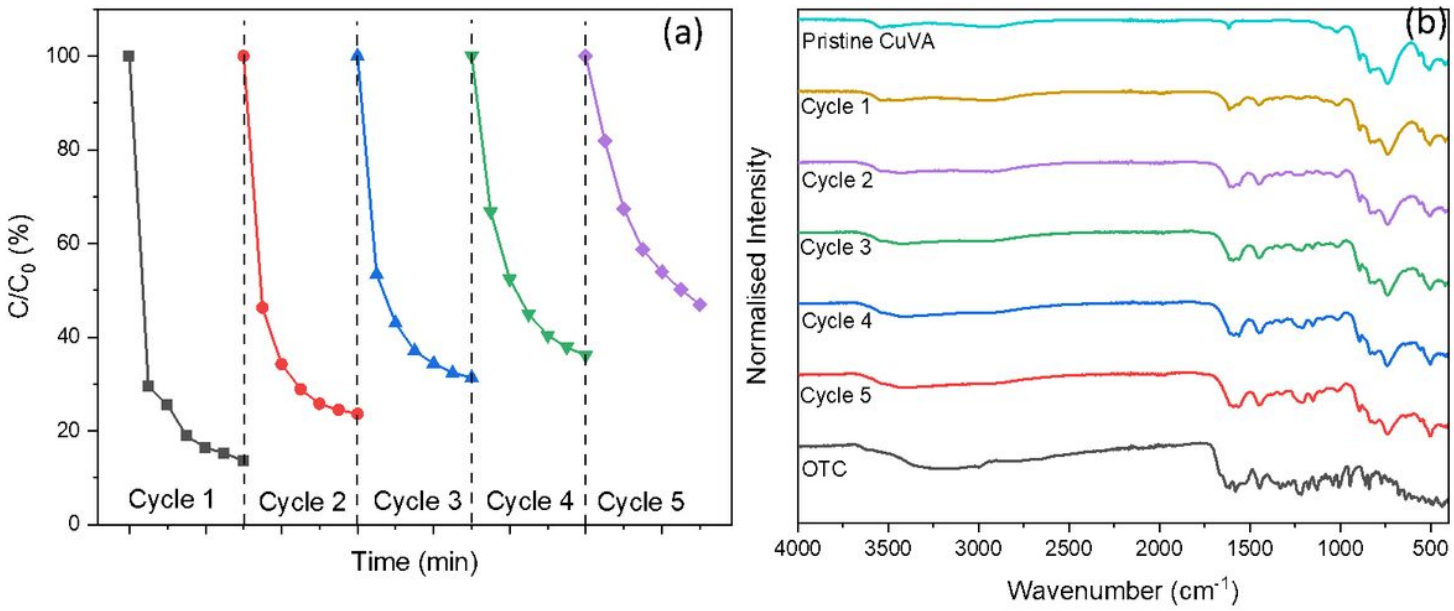


**Figure 10**

(a) Life cycle assessment of CuVA towards OTC for 5 cycles, and (b) FTIR spectra of recovered spent CuVA of respective cycles and OTC.

# Supplementary Files

This is a list of supplementary files associated with this preprint. Click to download.

- Supplementaryinformationlatest.docx